



HAL
open science

Numerical modelling of foam Couette flows

Ibrahim Cheddadi, Pierre Saramito, Christophe Raufaste, François Graner,
Philippe Marmottant

► **To cite this version:**

Ibrahim Cheddadi, Pierre Saramito, Christophe Raufaste, François Graner, Philippe Marmottant.
Numerical modelling of foam Couette flows. 2008. hal-00240536v1

HAL Id: hal-00240536

<https://hal.science/hal-00240536v1>

Preprint submitted on 6 Feb 2008 (v1), last revised 11 Jul 2008 (v2)

HAL is a multi-disciplinary open access archive for the deposit and dissemination of scientific research documents, whether they are published or not. The documents may come from teaching and research institutions in France or abroad, or from public or private research centers.

L'archive ouverte pluridisciplinaire **HAL**, est destinée au dépôt et à la diffusion de documents scientifiques de niveau recherche, publiés ou non, émanant des établissements d'enseignement et de recherche français ou étrangers, des laboratoires publics ou privés.

Numerical modelling of foam Couette flows

I. Cheddadi¹, P. Saramito¹, C. Raufaste^{2 a}, P. Marmottant², and F. Graner²

¹ CNRS, INRIA and Laboratoire Jean Kuntzmann, B.P. 53, 38041 Grenoble Cedex 9, France

² CNRS and Laboratoire de Spectrométrie Physique, B.P. 87, F-38402 St Martin d'Hères Cedex, France

February 6, 2008

Abstract. In this paper, a numerical simulation based on a tensorial elastoviscoplastic model is compared to experimental measurements on liquid foams for a bidimensional Couette flow, both in stationary and transient cases. The main features of the model are elasticity up to a plastic yield stress and viscoelasticity above. The numerical modelling bases on a small set of standard material parameters that could be fully characterised. Shear localisation as well as fine transient observations are reproduced and are found to be in good agreement with experimental measurements. The effect of the friction of plates is taken into account. The plasticity appears to be the fundamental mechanism of the localisation of the flow. Finally, the present approach could be extended from liquid foams to similar materials such as emulsions, colloids or wet granular materials, that exhibits localisations.

PACS. 47.57.Bc Foams and emulsions – 83.60.La Viscoplasticity; yield stress – 83.60.Df Nonlinear viscoelasticity – 02.60.Cb Numerical simulation; solution of equations – 07.05.Tp Computer modelling and simulation

Introduction

The bidimensional Couette flow of a foam has been widely studied, from experimental, theoretical and numerical point of view. Many studies focus on the velocity profile that could localise near the moving walls [1–3]: the measurements exhibits the coexistence between a flowing state and a solid state, similar to that observed for bi- or tridimensional shear flows of emulsions [4], colloids [5] or wet granular materials [6–9].

Most of these studies reveal either a continuous [6–8, 1] or discontinuous [4, 5, 2] transition between the flowing and solid state. These differences haven't been understood yet and continue to excite debate [2, 10]. A scalar elastoviscoplastic model including viscous drag was presented [11, 12]; it successfully reproduced the exponential decay of velocity that was observed in the bidimensional plane [10] and cylindrical [1] Couette flow of a foam between two glass plates. In both cases, the localisation was interpreted as the competition between the internal viscosity of the foam and the external friction from the glass plates. Recently, the data presented in [1] were re-analysed in [13] and, in addition to the velocity field, two tensorial informations were extracted both in stationary and transient regimes: the statistical elastic strain tensor and the plastic

rearrangements rate tensor which measures the plasticity. Up to now, these measurements haven't been compared to a numerical model.

The aim of this paper is to compare the measurements on a bidimensional Couette flow of a liquid foam between two glass plates presented in [1, 13] with the present numerical simulations based on a recent general tensorial and tridimensional elastoviscoplastic model [14] that combines viscoelasticity and viscoplasticity in the same framework. This model, which obeys by construction to the second principle of thermodynamics, leads to numerically stable equations and robust resolution algorithms. It is general enough to apply to both bi- and tridimensional geometries and to several materials. Here, it is applied to bidimensional foams using three parameters found in the literature (with only minor adjustments) and find a good agreement with the published experiments. This implies we can also use it to predict flows in several geometries and conditions, including transient, steady and oscillatory flows, even if no experiment is available.

The bidimensional Couette flow experimental set-up is briefly recalled in the first section. The second section presents the numerical modelling. The numerical results are then analysed and compared with data measurements in the third section for the transient case and in the fourth section for the stationary case. Finally, the last section explores the mechanism of localisation.

^a Present address: C. Raufaste, Physics of Geological Processes, University of Oslo, Sem Selands vei 24 NO-0316 Oslo, Norway

Correspondence to: pierre.saramito@imag.fr

1 Presentation of the experimental set-up

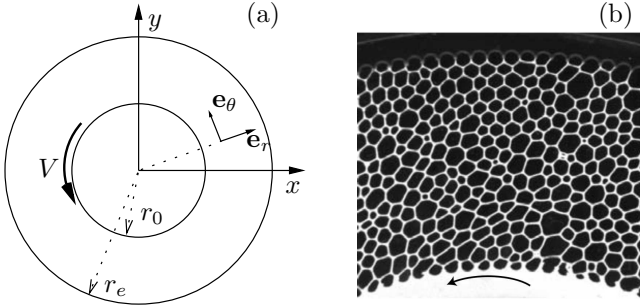


Fig. 1. Experimental set-up: (a) definition of the geometrical and kinematic parameters ; (b) picture of the confined bidimensional liquid foam (from [1]).

The experimental set-up is represented on Fig. 1. It consists of an inner shearing wheel of radius r_0 and an outer fixed one of radius r_e . Let $\Delta r = r_e - r_0$ denote the cylinder gap. The cylinder boundaries are tooth shaped and there is no slip. The liquid fraction of the foam is 5.2% and the bubble size is of the order 2 mm. The foam is confined between two transparent glass plates separated by an interval $h = 2$ mm. The inner wheel rotates at $V = 0.25 \text{ mm} \cdot \text{s}^{-1}$.

Two experimental runs are available:

- **Run 1** is related to the **transient case** and measurements are available in [13]. The internal radius is $r_0 = 71$ mm and the external radius is $r_e = 112$ mm. To prepare the foam, the inner disk is rotated counterclockwise, until a stationary regime is reached; then, at an arbitrary time chosen as the origin ($t = 0$), the shear direction is switched to clockwise, the experiment begins and measurements are made using image analysis. In [13], the measured quantities are averaged over eight equispaced orthoradial circular boxes corresponding to positions $r_j = r_0 + 1.7 \cdot 10^{-3} \times (0.4 + 2.7 \times (j - 0.5))$ for $j = 1$ to 8.

- **Run 2** focuses on the **stationary case** and measurements are presented in [1, 13, 15]. The internal radius is $r_0 = 71$ mm, as for the previous run, and the external radius is $r_e = 122$ mm, which differs from the previous run. The preparatory rotation is clockwise. Then, at an arbitrary time, it is switched to counterclockwise. Pictures are recorded only after a full 2π turn.

2 The numerical modelling

The strain tensor ϵ is supposed to split into two contributions:

$$\epsilon = \epsilon^{(p)} + \epsilon^{(e)}, \quad (1)$$

where $\epsilon^{(p)}$ and $\epsilon^{(e)}$ denote respectively the plastic and the elastic strain tensors. The model considered in this pa-

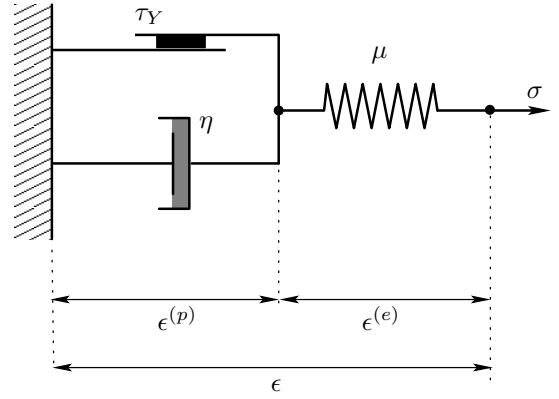


Fig. 2. The elastoviscoplastic model.

per is presented on Fig. 2. The total Cauchy stress tensor writes:

$$\sigma = -p \mathbf{I} + \tau,$$

where p is the pressure, \mathbf{I} is the identity tensor in two dimensions, $\tau = 2\mu\epsilon^{(e)}$ is the elastic stress tensor, and μ is the elastic modulus of the foam. When the stress is lower than a yield value, the material behaves as an elastic solid: the plastic strain $\epsilon^{(p)}$ is equal to zero and the stress is $2\mu\epsilon$. Otherwise, the foam is supposed to behaves as a Maxwell viscoelastic fluid with a relaxation time $\lambda = \eta/\mu$, where η is the viscosity. This model is a simplified version of the model introduced in [14]: the second *solvent* viscosity of the original model is here taken to zero. This choice is coherent with experimental observations [13, 3]: at slow rates of strain, when no plasticity occurs, the foam behaves as a solid elastic body while the model considered in [14] describes a more general Kelvin-Voigt viscoelastic solid. This choice in the modelling is also justified *a posteriori* in the present paper by comparisons between numerical simulations and experimental measurements. The tensor τ satisfies the following nonlinear differential constitutive equation:

$$\lambda \frac{D\tau}{Dt} + \max\left(0, 1 - \frac{\tau_Y}{|\tau_d|}\right) \tau = 2\eta \mathbf{D}(\mathbf{v}), \quad (2)$$

where \mathbf{v} is the velocity field, $\mathbf{D}(\mathbf{v}) = (\nabla \mathbf{v} + \nabla \mathbf{v}^T)/2$ is the rate of strain tensor and $\tau_Y > 0$ is the yield stress constant. We denotes also $\tau_d = \tau - (1/2) \text{tr}(\tau) \mathbf{I}$ the deviatoric part of τ and $|\tau_d|$ its matrix norm. The upper convected derivative of tensors writes :

$$\frac{D\tau}{Dt} = \frac{\partial \tau}{\partial t} + (\mathbf{v} \cdot \nabla) \tau - \tau \nabla \mathbf{v}^T - \nabla \mathbf{v} \tau$$

The problem is completed by the conservation of momentum:

$$\rho \left(\frac{\partial \mathbf{v}}{\partial t} + \mathbf{v} \cdot \nabla \mathbf{v} \right) - \text{div} \sigma = -\frac{\beta}{h} \mathbf{v}, \quad (3)$$

where ρ denotes the constant density. The right-hand side expresses the external force due to the friction of the plates: $\beta \geq 0$ is a friction coefficient and h the distance

between the two plates. Following [11], a linear friction model is assumed. Finally, since the density is supposed to be constant, the mass conservation reduces to :

$$\operatorname{div} \mathbf{v} = 0. \quad (4)$$

The three unknowns of the problem are $(\boldsymbol{\tau}, \mathbf{v}, p)$ and the corresponding equations are (2), (3) and (4). The problem is closed by some boundary conditions for \mathbf{v} at $r = r_0$ and r_e for any $t > 0$ and some initial conditions for $\boldsymbol{\tau}$ and \mathbf{v} . In the bidimensional polar coordinate system (r, θ) , the solution is assumed to be independent of θ : the radial component velocity v_r is zero and v_θ is simply written as v . The problem reduces to a time-dependant one-dimensional system of partial derivative equation with four unknowns v , τ_{rr} , $\tau_{r\theta}$, $\tau_{\theta\theta}$ that depend upon t and r . The problem is then solved using an operator splitting algorithm and a finite element method that are similar to those used for viscoelastic fluid flow problems [16]. The details of the numerical algorithms will be detailed in a separate paper.

In order to perform computations and compare it to the experimental data, in addition to the numerical values of the kinematic and geometric parameters $(V, \Delta r, h)$ of the experimental set-up, the quantification of the material parameters $(\mu, \eta, \tau_Y, \beta)$ of the model is also required. Let Δr , V , $\Delta r/V$ and $\eta V/\Delta r$ be respectively the characteristic length, velocity, time and stress. The problem involves only three dimensionless numbers, the Bingham, the Weissenberg and a friction numbers, defined by:

$$Bi = \frac{\tau_Y \Delta r}{\eta V}, \quad We = \frac{\eta V}{\mu \Delta r} \quad \text{and} \quad C_F = \frac{\beta \Delta r^2}{\eta h} \quad (5)$$

Notice that this choice of dimensionless numbers corresponds to a description of the foam as a fluid: the characteristic stress is a viscous stress. An alternative choice would be to choose the elastic modulus μ as the characteristic stress in order to emphasise the solid-like behaviour of the foam; the corresponding dimensionless numbers would be the yield deformation $\epsilon_Y^{(e)} = Bi We = \frac{\tau_Y}{\mu}$ instead of the Bingham number, the ratio $\frac{\beta V \Delta r}{\mu h} = C_F We$ of the friction of the plates with the elastic modulus instead of C_F , and the same Weissenberg number. However, with this choice, we cannot reach the viscoplastic limit. Thus, the first choice (Bi, We, C_F) is more general and we will present the numerical results as a function of these parameters. From [15], the bidimensional elastic modulus in $\text{N} \cdot \text{m}^{-1}$ expresses $\bar{\mu} = \mu/h \approx 2 \cdot 10^{-2}$. The estimation of the elastic modulus μ in $\text{N} \cdot \text{m}^{-2}$ is $\mu \approx 10 \text{ N} \cdot \text{m}^{-2}$. From [3] the relaxation time $\lambda = \eta/\mu$ of the foam on this experiment should be of the order of 1 s and then $\eta \approx 10$ Pois. The dimensionless quantity $\epsilon_Y^{(e)}$ is evaluated from the experiments as the maximal value of $|\epsilon_d^{(e)}|$ and then $\epsilon_Y^{(e)} \approx 0.26$. It should be pointed out that, in the model, $\epsilon_Y^{(e)}$ is the value of $|\epsilon^{(e)}|$ at which plasticity occurs and thus $|\epsilon_d^{(e)}|$ can exceed $\epsilon_Y^{(e)}$. Thus $\tau_Y \approx 5.2 \text{ N} \cdot \text{m}^{-2}$. Also from [15],

the friction force at the plates is estimated in $\text{N} \cdot \text{m}^{-2}$ for any velocity v as $f = 31 v^{0.64}$. Since the maximum value of the velocity is $V = 0.25 \text{ mm/s}$, the maximum value of the friction force is $31 \times (0.25 \cdot 10^{-3})^{0.64}$. Following [11], a linear friction model is assumed: $\tilde{f} = \beta v/h$, where β is chosen such that the maximal value of the friction is the same with the two expressions: $\beta \approx 31 \times (0.25 \cdot 10^{-3})^{0.64} / (0.25 \cdot 10^{-3}) = 613 \text{ Pois} \cdot \text{m}^{-1}$. After a first computation based on this set of parameters, a little adjustment was necessary to compare better with the experimental data. The following set of parameters leads to a good agreement of the model with *both* transient and stationary cases: $\mu = 10.9 \text{ N} \cdot \text{m}^{-2}$, $\eta = 13.1$ Pois, $\tau_Y = 5.47$. $\beta = 613 \text{ Pois} \cdot \text{m}^{-1}$. All the comparisons between numerical computations and experimental measurements presented in this paper are performed with this set of parameters. This adjustment leads to the set of dimensionless numbers presented in Table 1, as defined in (5). Since the nonlinear inertia term $\mathbf{v} \cdot \nabla \mathbf{v}$

run	Bi	We	C_F
1. transient	68.3	7.31×10^{-3}	39.2
2. stationary	85.0	5.88×10^{-3}	60.7

Table 1. The choice of dimensionless numbers as defined in (5). The material parameters of the foam are identical. Since the cylinder gap differs between the two runs, the dimensionless numbers are slightly different between the two runs.

in (3) vanishes for simple shear flows such as the Couette flow, the Reynolds number $Re = \rho V \Delta r / \eta \approx 5 \times 10^{-5}$ has a negligible influence on the transient problem and no influence on the stationary one. Thus, Re is taken as zero for the simulations. For the comparison with experiments, the results at time t and radius r is expressed in a dimensionless form, respectively, as the total applied shear $\gamma = Vt/\Delta r$ and as the distance to the inner cylinder normalised by the size of the gap $(r - r_0)/\Delta r$.

3 The transient flow simulation

The transient numerical simulation is performed in the following way: first, the simulation is done with the foam initially at the rest and, for $t > 0$, with $v(r_0) = V$ and $v(r_e) = 0$. When a stationary regime is reached, the boundary conditions are changed to $v(r_0) = -V$ and $v(r_e) = 0$ and computations are stored at each time.

Fig. 3.a plots the velocity profile versus r at different fixed times. Conversely, the velocity is represented on Fig. 3.b versus the times at different fixed radius, from $r = r_1$ to r_8 . At the beginning of the transient, when $\gamma = 0.01$, the shear direction has just switched and the velocity profile is roughly exponential. After a short transition, $0 \leq \gamma \leq 0.1$, the velocity profile becomes quasi-linear up to $\gamma \approx 0.3$. Then, at $\gamma = 0.3$ and $r = r_1$, i.e. near the

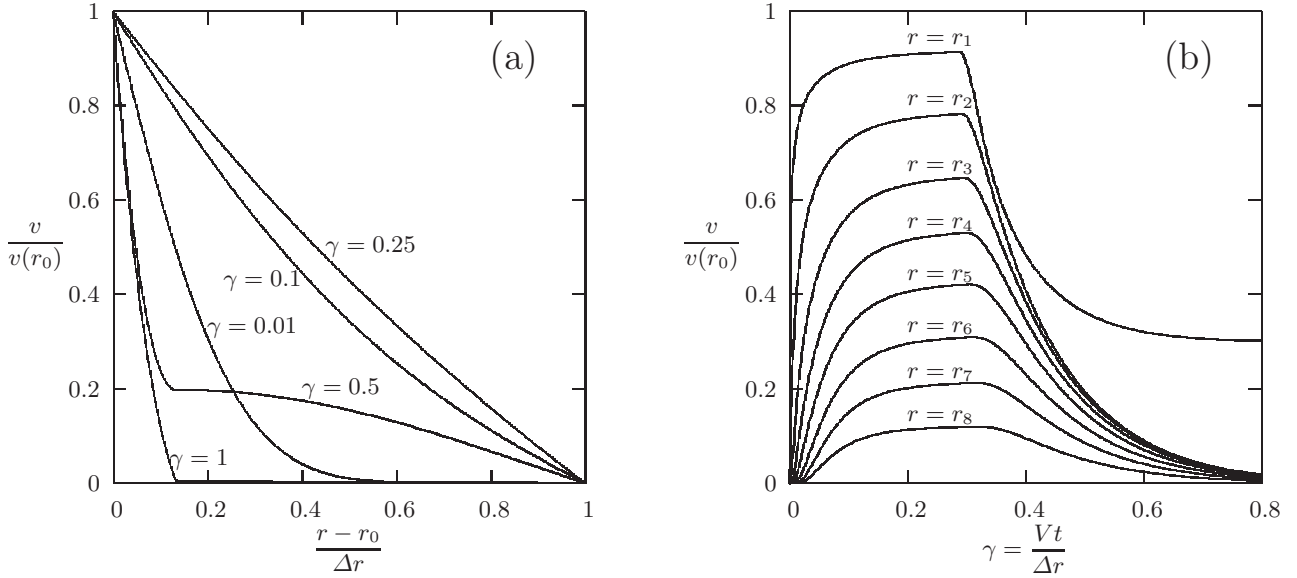


Fig. 3. Transient case: (a) velocity profile versus r at different times ; (b) velocity profile versus t for $r = r_1$ to r_8 .

moving disk, it starts to decrease rather abruptly. Far from the moving disk, the decrease starts later, at $\gamma = 0.35$. At $\gamma = 1$, the foam has reached a stationary regime in which the flow is strongly localised near the moving disk.

Fig 4 shows the cross component of $\epsilon_{r\theta}^{(e)} = \tau_{r\theta}/(2\mu)$ versus time at fixed radius $r = r_1$ to r_8 . After a short transition of about 0.05, $\epsilon_{r\theta}^{(e)}$ reaches a first regime where it varies linearly ($0.05 \leq \gamma \leq 0.3$ for $r = r_1$ and $0.2 \leq \gamma \leq 0.4$ for $r = r_8$). Notices that the dimensionless time γ interprets also as the applied strain. Thus, the stress τ depends linearly upon γ i.e. the material behaves as an elastic solid in this regime. Then, after a second transition, the flow reaches a second regime that is the stationary one. For a fixed radius r , the characteristic value of γ associated to this second transition is denoted by $\gamma_c(r)$. It is defined by the intersection between the first linear regimes and the second asymptotic one, as shown in the inset of Fig. 4.

Then, γ_c is represented versus the radius and compared to experimental data from [13] on Fig. 5.a. Remarks that all the values predicted by the numerical modelling are in the error margin of the experiment. Both for the experiment and the numerical simulation, the value of γ_c increases gradually with r and this variation is linear. A linear regression procedure leads to $\gamma_c(r) \approx \alpha \frac{r-r_0}{\Delta r} + \gamma_c^{(0)}$ with $\alpha = 0.49$. Here, $\gamma_c^{(0)}$ is associated to the first transition regime and depends upon the initial conditions. Recall that when the slope α is not vanishing, the region close to the moving disk saturates earlier than the region far from it. Let us study how the slope α is influenced by the values of the parameters. As the foam behaves like an elastic solid during transient, we find more adequate to study this dependency with respect to $(Bi We, C_F We, We)$ as has been already discussed in section 2. On the one hand, when either Bi varies in the range $[0 : 137]$ or We in the

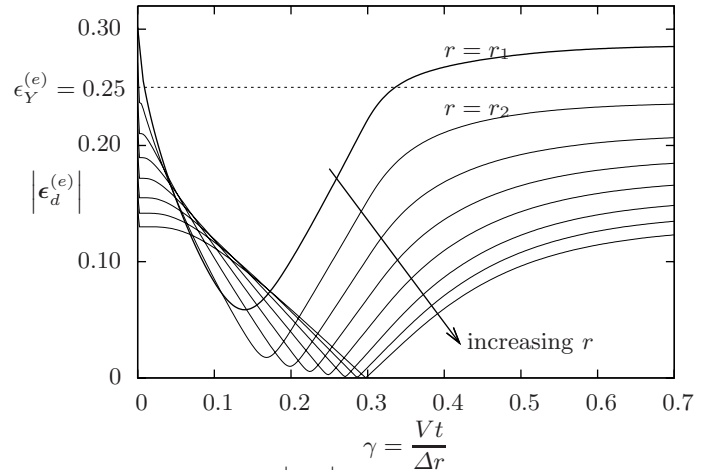


Fig. 6. Transient case: $|\epsilon_d^{(e)}|$ versus t for different values of r from $r = r_1$ to r_8 .

range $[0 : 0.25]$ and the product $C_F We = 0.287$ is maintained constant, the relative variation of α is less than 6%. On the other hand, when both Bi and We are fixed as in Table (1), and only the product $C_F We$ alone varies from 0 to 0.6 then the slope varies linearly as $\alpha = 1.42 C_F We$, as shown on Fig. 5.b. Clearly, the slope α is governed by the product $C_F We = \frac{\beta V \Delta r}{\mu h}$: it is proportional to the drag coefficient β and inversely proportional to the elastic modulus μ . Finally:

$$\gamma_c(r) \approx 1.42 C_F We \left(\frac{r-r_0}{\Delta r} \right) + \gamma_c^{(0)}$$

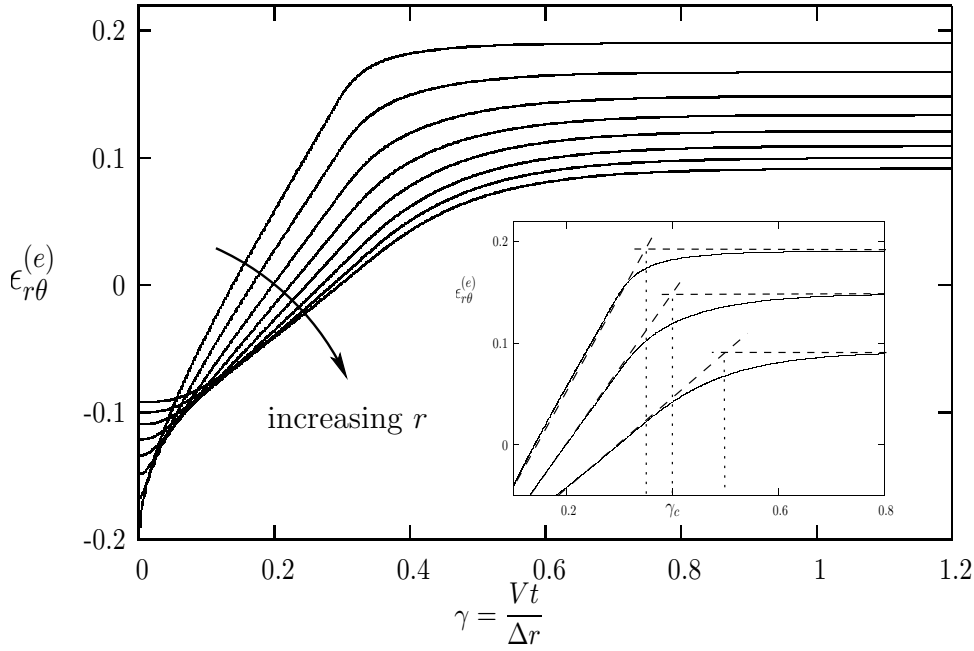


Fig. 4. Transient case: cross component of the elastic strain $\epsilon_{r\theta}^{(e)}$ vs t for $r=r_1$ to r_8 . In the inset, the vertical dashed lines mark the cross-over γ_c between the transient and the stationary regimes, defined by the intersection of the asymptotic value of $\epsilon_{r\theta}^{(e)}$ and the linear regression of $\epsilon_{r\theta}^{(e)}$ in the first regime.

Fig. 6 plots the norm of the deviatoric part of the elastic strain tensor

$$\left| \epsilon_d^{(e)} \right| = \left(2 \left(\epsilon_{r\theta}^{(e)} \right)^2 + \frac{1}{2} \left(\epsilon_{rr}^{(e)} - \epsilon_{\theta\theta}^{(e)} \right)^2 \right)^{\frac{1}{2}}.$$

Recall that $\epsilon^{(e)} = \tau / (2\mu)$ and that the plasticity occurs when $|\tau_d| \geq \tau_Y$. Thus the plasticity occurs when $|\epsilon_d^{(e)}|$ is above $\epsilon_Y^{(e)} = \tau_Y / (2\mu) = BiWe/2 = 0.25$. Fig. 6 shows that this situation appears only close to the moving cylinder, for $r=r_1$, and only for small times, during the first transition regime, and for large time, during the stationary regime. At initial time, $|\epsilon_d^{(e)}|$ is above $\epsilon_Y^{(e)}$ near the moving disk. As the disk moves, the velocity and its gradient change of sign and $|\epsilon_d^{(e)}|$ decreases rapidly until $|\epsilon_d^{(e)}| < \epsilon_Y^{(e)}$ everywhere in the foam. Therefore there is no plasticity in the foam and the constitutive equation writes also: $\frac{D\epsilon^{(e)}}{Dt} = D(\mathbf{v})$. This relation expresses that all the velocity gradient is loaded into $\epsilon^{(e)}$. The foam behaves like an elastic body and $\epsilon_{r\theta}^{(e)}$ increases linearly with the applied strain γ . Because of the cylindrical geometry and the friction of the plates, $\epsilon^{(e)}$ is higher near the inner moving disk. When $|\epsilon_d^{(e)}|$ reaches $\epsilon_Y^{(e)}$ near the inner disk, plasticity occurs and the foam starts to flow. Then $\epsilon^{(e)}$ saturates everywhere in the gap even though it is above the yield deformation only in a region near the moving disk. Inside this region, the foam is flowing while outside, there is no flow and the foam is at the rest.

Let us summarise the situation for the transient case. After a brief transition, the material behaves as an elastic solid: there is no plasticity yet and the velocity profile is quasi linear. The deformation saturates first near the moving disk, and then gradually throughout the gap. The friction of the plates is responsible for this gradual saturation. Finally, after this second transition, the stationary regime is reached: the material is flowing and the flow is strongly localised near the moving disk.

4 The stationary flow simulation

The stationary numerical simulation is performed in the following way: at $t=0$, the foam is at rest, all variables are set to zero. For $t > 0$ the inner cylinder moves and the boundary conditions are $v(r_0)=V$ and $v(r_e)=0$. The computation is performed until the stationary regime is reached.

Fig. 7.a compares the numerical results to measurements made in [1]. The velocity is strongly localised near the moving disk, as it was already observed in the transient case on Fig. 3.b. Both the computed and the experimental velocities have the same initial slope, but the transition to zero is more abrupt in the case of the numerical resolution. Let us denote r_c the radius where the velocity drops to zero. The computation gives $r_c=77.6$ mm while $r_c=84.0$ mm for the experimental data. The r_c prediction error is of about 12 % of the gap size.

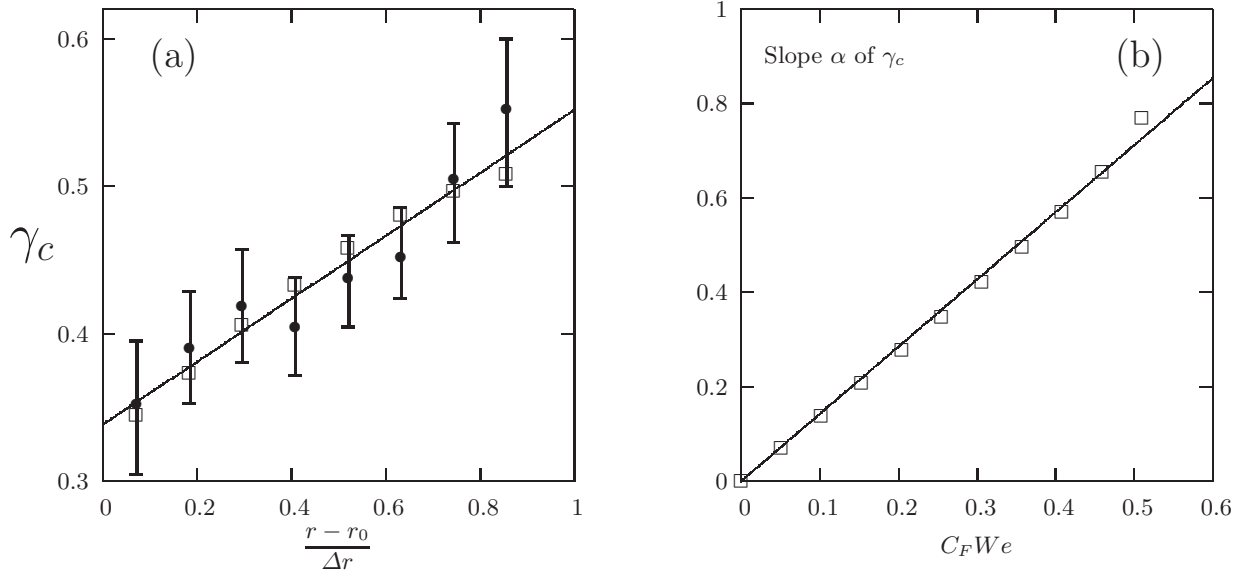


Fig. 5. Transient case: (a) γ_c vs r . The points \bullet with error bars are experimental data while the \square are numerical prediction data and the solid line is a linear regression on these numerical data. (b) Influence of C_F on the slope α of γ_c . The \square are data from numerical simulation and the solid line is a linear regression on these numerical data.

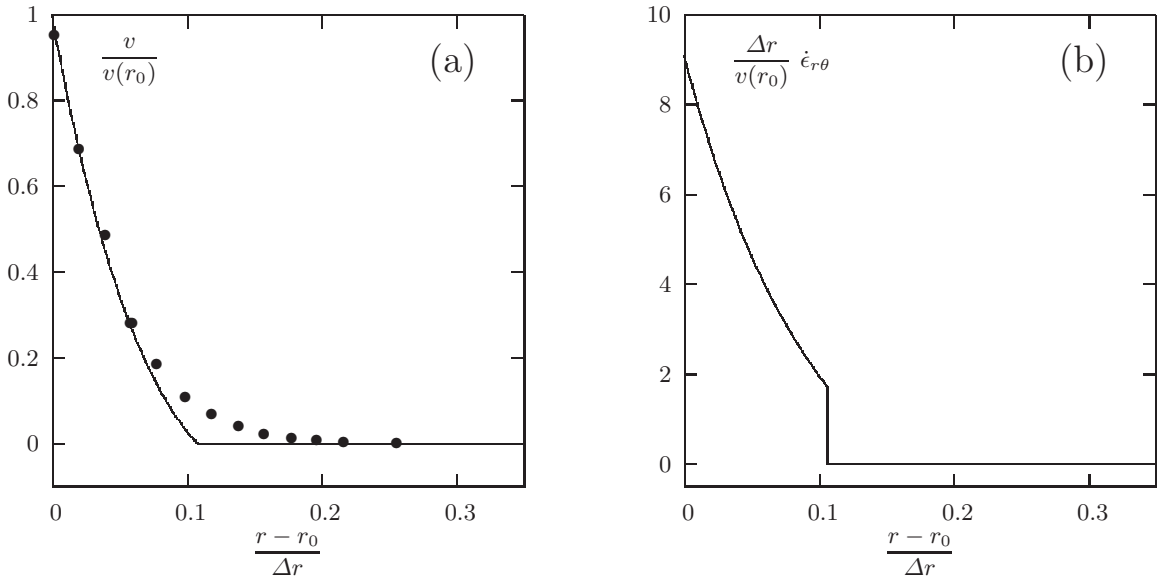


Fig. 7. Stationary case: (a) Velocity versus r . The curve is the computed velocity while the \bullet points are experimental data from [1]. (b) Shear strain rate $\dot{\epsilon}_{r\theta}$ vs r .

Fig. 7.b represent the total shear strain rate $\dot{\epsilon}_{r\theta}$. However, the computed rate of strain exhibits an interesting feature: it strongly localised near the moving disk and also discontinuous at the transition between the flowing state at the jammed state. There is no experimental data available for the comparison.

Finally, the stationary elastic strain $\epsilon^{(e)}$ is compared to experimental measurements from [17] for both the shear component $\epsilon_{r\theta}^{(e)}$ (Fig. 8.a) and the difference of normal

components $\epsilon_{rr}^{(e)} - \epsilon_{\theta\theta}^{(e)}$ (Fig. 8.b). The computed $\epsilon_{r\theta}^{(e)}$ is slightly overestimated. Nevertheless, it presents qualitatively the same behaviour as the experimental one: it does not localise near the moving disk and it varies smoothly with r . The computed difference of the normal components $\epsilon_{rr}^{(e)} - \epsilon_{\theta\theta}^{(e)}$ presents a discontinuity at the point at $r = r_c$, where the computed velocity and plasticity drop to zero. The sign of the experimental data changes in the middle of the gap. Experimental data could display measurement artefacts [13], but anyway it is not surprising

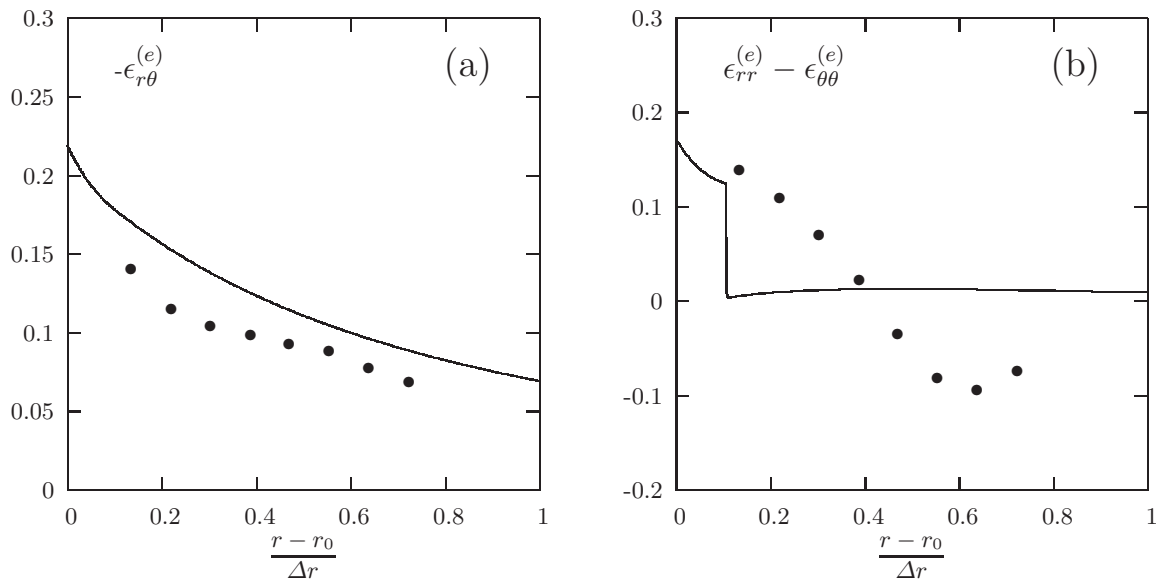


Fig. 8. Stationary case: Solid line is the numerical resolution while \bullet points are experimental data from [13]. (a) Shear component $-\epsilon_{r\theta}^{(e)}$ vs r . (b) Difference of normal components $\epsilon_{rr}^{(e)} - \epsilon_{\theta\theta}^{(e)}$ vs r .

that the two data sets could not be compared quantitatively: since $\epsilon_{rr}^{(e)} - \epsilon_{\theta\theta}^{(e)}$ is not so geometrically constrained as is $\epsilon_{r\theta}^{(e)}$, this quantity depends on the initial conditions, especially in the *unshaked* solid region. Actually anisotropic trapped elasticity may be initially present in the experimental setup [18], which is not considered in the model.

Compared to experimental measurements, the computed data exhibit a rather discontinuous transition from flowing to jammed behaviour, in particular a discontinuity in the rate of strain and in the difference of the normal stress components. The origin of this abrupt predicted behaviour is also not yet clearly elucidated. We recall that such an abrupt transition has been observed on bubble rafts [2] and various experimental systems [4, 5]. This problem will be addressed in future works.

5 The mechanism of localisation

In order to probe the effect of the friction of the plates on the localisation in the stationary regime, a stationary numerical resolution with both $Bi = 85.0$ and $We = 5.88 \times 10^{-3}$ unchanged, and C_F set to zero, is performed. The result is compared on Fig. 9.a to the numerical solution with the reference set of parameters $C_F = 60.7$ from Table (1). Observe that the velocity profile is almost the same: the friction of the plates doesn't seem to be responsible of the localisation in this experiment. The dependence of the localisation point r_c upon We was found to be negligible. More precisely, for any fixed value of Bi in the range $[0 : 153]$, the variation of $r_c/\Delta r$ upon We in the range $[0 : 1.96 \times 10^{-2}]$ was found to be less than 3%. Thus,

the localisation point r_c could be approximated by using the Bingham model. Fig. 9.b plots the localisation point versus Bi for the Bingham model ($We = C_F = 0$). Observe that $r_c - r_0$ behaves as $Bi^{-1/2}$. An explicit computation for the Couette flow of a Bingham fluid (see e.g. [19] or [20, p. 241]) expresses the ratio r_c/r_0 as the solution of:

$$\left(\frac{r_c}{r_0}\right)^2 - 2 \ln\left(\frac{r_c}{r_0}\right) = 1 + 2\sqrt{2} \left(\frac{\Delta r}{r_0}\right) Bi^{-1}$$

A Taylor expansion for small $r_c - r_0$ leads to:

$$\frac{r_c - r_0}{\Delta r} \approx 2^{1/4} \left(\frac{r_0}{\Delta r}\right)^{1/2} Bi^{-1/2}. \quad (6)$$

This explicit approximate formulæ is of practical interest for the prediction on the localisation point, as shown on Fig. 9.b.

In [10], the authors shear a bubble raft in a *plane* Couette geometry and see no localisation at all. Adding a plate on the top, a localisation is observed. The authors conclude that the plate is responsible for the localisation. This result seems to be in contradiction with the previous conclusion, where the friction was found to have a minor influence on the localisation. However, the geometry is not the same. We performed the numerical resolution of our model in the case of a plane Couette flow in order to check if our model was able to reproduce the behaviour observed in [10]. A gap width of 40 mm and a moving boundary with a velocity of 0.25 mm/s were used for the numerical resolution, so that we have geometrical parameters similar to [10]. The dimensionless numbers $Bi = 85$ and $We = 5.88 \times 10^{-3}$ are fixed and only C_F is varying. Fig. 10 shows the results for of $C_F = 0, 6.07$ and 60.7 . For $C_F = 0$, all the foam is flowing and the velocity profile is

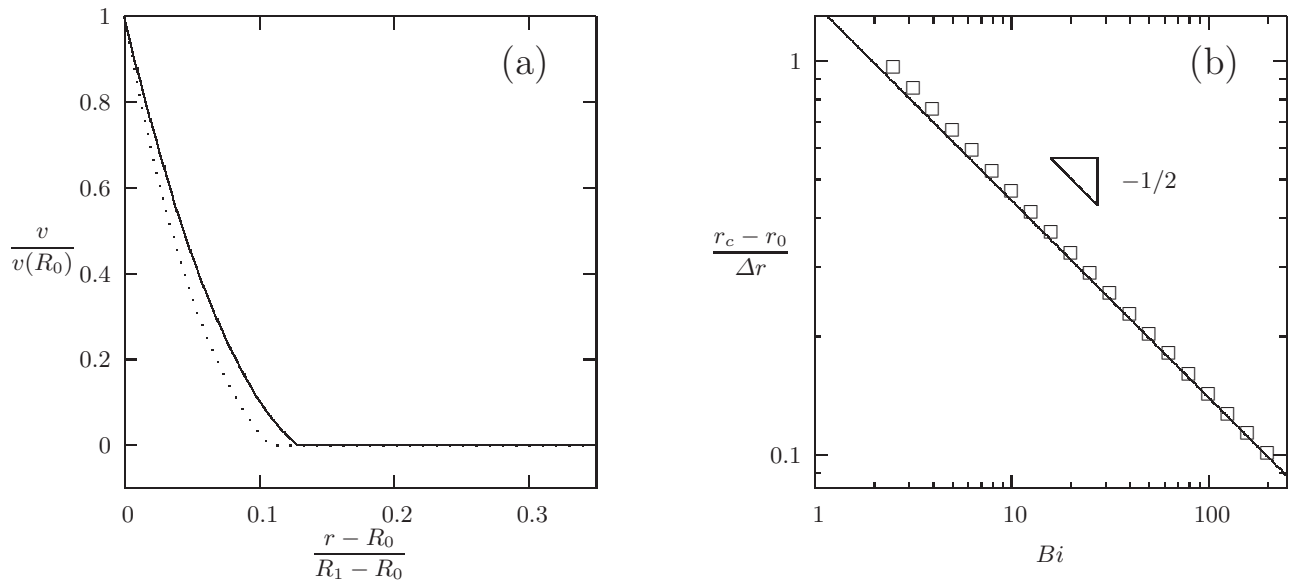


Fig. 9. Stationary case: (a) velocity profile for $Bi=85$, $We=5.88 \times 10^{-3}$ and both $C_F=0$ (solid curve) and $C_F=60.7$ (dashed curve). (b) Localisation point vs Bi for the stationary Bingham fluid ($We = C_F = 0$): points \square are obtained by an exact computation while the solid line represents the approximate formulae (6).

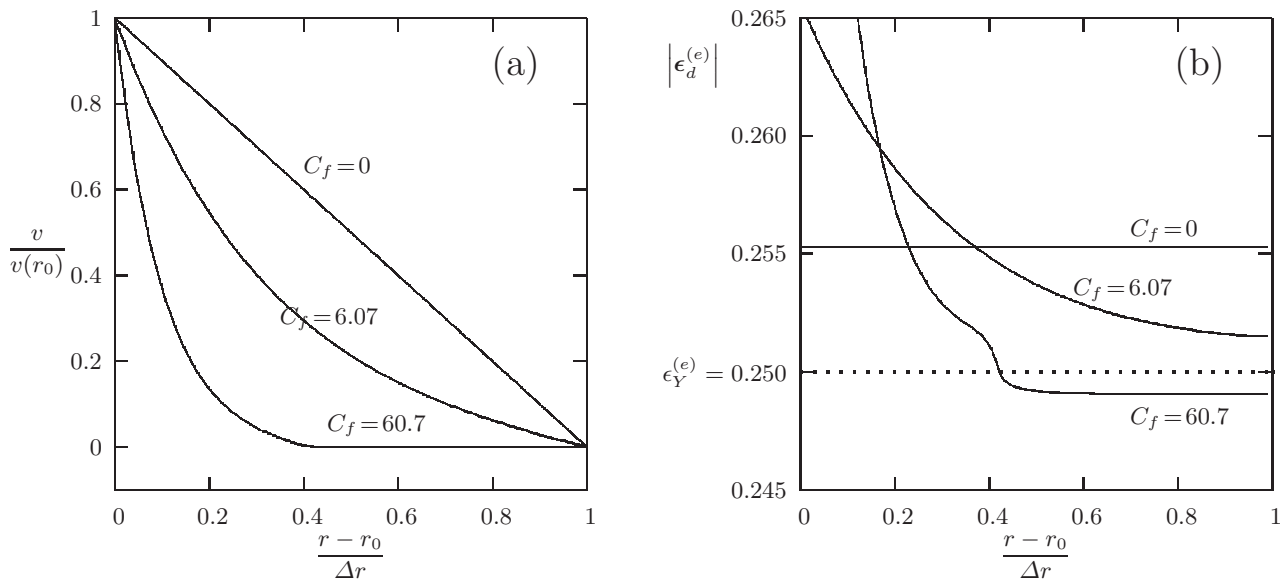


Fig. 10. Stationary plane Couette case with $Bi=85$, $We=5.88 \times 10^{-3}$ and C_F varying: (a) velocity profile ; (b) $|\epsilon_d^{(e)}|$.

linear (Fig. 10.a) while $|\epsilon_d^{(e)}|$ is constant and above $\epsilon_Y^{(e)}$ (Fig. 10.b). For $C_F=6.07$, all the foam is flowing but the velocity profile is no more linear while $|\epsilon_d^{(e)}|$ is non uniform but above $\epsilon_Y^{(e)}$ throughout the gap. For $C_F=60.7$, the velocity is localised in the 42 % left region of the gap while $|\epsilon_d^{(e)}|$ is not uniform: it is above $\epsilon_Y^{(e)}$ in the region adjacent to the moving plane and under $\epsilon_Y^{(e)}$ otherwise.

As a main conclusion of this paragraph, we do not explain the localisation by the competition between an internal viscosity and an external friction as in [12], but rather by the non uniform stress and the simple picture that part of the system is above the yield stress and part of the system is below the yield stress. In the case of the *plane* Couette flow, the friction of the plates is responsible for the non uniform stress, whereas in the case of the *cylindrical* Couette flow, it is mostly the geometry. In addition, in this case, the localisation position is mainly governed

by the Bingham number while both the friction and the Weissenberg number have only a minor influence.

Conclusion

For the first time, comparisons between an elastoviscoplastic model and measurements both in stationary and transient cases are performed and found to be in good agreement. The direct numerical resolution allows a full comparison with all available data from measurement. The comparison was performed with only one set of material parameters: it confirms the predictive character of the proposed model. This model is fully parametrised by only three standard dimensionless numbers. These numbers depend on a limited set of material parameters that could be quantified by some measurements.

The transition to the shear banding was analysed both in the transient and stationary cases: an elastic behaviour during the transient flow is exhibited. The effect of the friction of plates on the propagation of the plastic rearrangements throughout the gap is also analysed in details. In the stationary case, a non uniform stress throughout the gap leads to a flowing part above the yield stress and a jammed part under the yield stress. It appears to be the fundamental mechanism for the localisation of the flow. The mechanism of localisation is analysed with details from two points of view: the effect of friction on the plates and the plasticity. Finally, the plasticity appears to be the fundamental mechanism of the localisation of the flow.

In the future, we plan to compare the numerical resolution of our model with more complex liquid foam flows like Stokes flows and flows around an obstacle [21, 22]. We will also try to have a better understanding of the abrupt jamming transition. Finally, we point out the fact that our approach is not specific to liquid foams: it could well describe emulsions, colloids or wet granular materials that are known to develop a similar behaviour.

Acknowledgements

We are extremely grateful to G. Debrégeas for providing us with many recordings of his published and unpublished experiments. We would also like to thank S. Cox, B. Dollet, E. Janiaud, and A. Wyn and the Foam Mechanics Workshop (Grenoble, January 2008) and all its participants for fruitful discussions.

References

1. G. Debrégeas, H. Tabuteau, J.M. di Meglio, Phys. Rev. Letter **87**(17) (2001)
2. J. Lauridsen, G. Chanan, M. Dennin, Phys. Rev. Lett. **93**(1), 018303 (2004)
3. A. Kabla, J. Scheibert, G. Debrégeas, J. of Fluid Mech. **587**, pp. 45 (2007)
4. P. Coussot, J.S. Raynaud, F. Bertrand, P. Moucheront, J.P. Guilbaud, H.T. Huynh, S. Jarny, D. Lesueur, Phys. Rev. Lett. **88**(21), 218301 (2002)
5. J.B. Salmon, A. Colin, S. Manneville, F. Molino, Phys. Rev. Lett. **90**(22), 228303 (2003)
6. D. Howell, R.P. Behringer, C. Veje, Phys. Rev. Lett. **82**(26), 5241 (1999)
7. D.M. Mueth, G.F. Debrégeas, G.S. Karczmar, P.J. Eng, S.R. Nagel, H.M. Jaeger, Nature **406**, 385 (2000)
8. W. Losert, L. Bocquet, T.C. Lubensky, J.P. Gollub, Phys. Rev. Lett. **85**(7), 1428 (2000)
9. N. Huang, G. Ovarlez, F. Bertrand, S. Rodts, P. Coussot, D. Bonn, Phys. Rev. Lett. **94**(2), 028301 (4) (2005)
10. Y. Wang, K. Krishan, M. Dennin, Phys. Rev. E **73** (2006)
11. E. Janiaud, D. Weaire, S. Hutzler, Phys. Rev. Lett. **97**(3), 038302 (2006)
12. R.J. Clancy, E. Janiaud, D. Weaire, S. Hutzler, Eur. Phys. J. E **21**(2), 123 (2006)
13. E. Janiaud, F. Graner, J. Fluid Mech. **532**, 243 (2005)
14. P. Saramito, J. Non Newtonian Fluid Mech. **145**(1), 1 (2007)
15. C. Raufaste, Ph.D. thesis, Université Joseph Fourier, Grenoble, France (2007), <http://tel.archives-ouvertes.fr/docs/00/19/32/48/PDF/TheseRaufaste.pdf>
16. P. Saramito, J. Non Newtonian Fluid Mech. **60**, 199 (1995)
17. P. Marmottant, C. Raufaste, F. Graner, *submitted* (2007), <http://hal.archives-ouvertes.fr/hal-00092006/fr>
18. V. Labiausse, R. Höhler, S. Cohen-Addad, J. Rheol. **51**, 479 (2007)
19. M. Fortin, D. Côté, P.A. Tanguy, Comput. Methods in Appl. Mech. and Eng. **88**, 97 (1991)
20. N. Roquet, Ph.D. thesis, Université Joseph Fourier, Grenoble, France (2000), <http://ljk.imag.fr/membres/Pierre.Saramito/Nicolas-Roquet-these.pdf>
21. N. Roquet, P. Saramito, Comput. Appl. Meth. Mech. Engrg. **192**(31-32), 3317 (2003)
22. B. Dollet, F. Graner, J. Fluid Mech. **585**, 181 (2007)